Other supplementary material

Mouad BOUDINA[1,2], Frédérick P. GOSSELIN[1,2] and Stéphane ÉTIENNE[1]

[1] Mechanical Engineering Department, Polytechnique Montréal, Montréal, Québec, Canada

[2] Laboratory for Multiscale Mechanics (LM2), Mechanical Engineering Department, Polytechnique Montréal, Montréal, Québec, Canada

Corresponding author: Mouad Boudina. Email address: mouad.boudina@polymtl.ca

1 Particle advection

The code PARADVECT [2020] integrates the momentum equation of a single particle (equations (3.13) in the main article) using a first order forward Euler scheme. To verify the code, we simulate the trajectories of two particles, a small one of diameter ratio $R = 0.01$ and a larger one of $R = 0.1$, advected by a uniform and unidirectional flow $\bar{\boldsymbol{U}} = \boldsymbol{e}_x$ in a domain without obstacles. The grid is the same in these two sets of simulations. We calculate the temporal discretisation error [Oberkampf and Roy, 2010] of the x coordinate of the particle path

$$\varepsilon_{\Delta t} = ||x_{0,2\Delta t} - x_{0,\Delta t}||_2 = \left[2\Delta t \sum_{i=1}^{N_\mathrm{f}/2} |x_{0,2\Delta t}(t_k) - x_{0,\Delta t}(t_k)|^2 \right]^{1/2}, \tag{1}$$

where the subscript $(.)_{.,\Delta t}$ refers to the solution with a time step equal to Δt.

The observed order of accuracy $\hat{p}_{\Delta t}$ is given by [Oberkampf and Roy, 2010]

$$\hat{p}_\Delta = \frac{\log(\varepsilon_\Delta / \varepsilon_{2\Delta t})}{\log(2)}. \tag{2}$$

The convergence results are plotted in figure 1. We obtained, as expected, a first order decrease in the discretisation error, and the observed order of accuracy is close to one for small time steps.

A validation of PARADVECT [2020] is given in Boudina et al. [2020], where the capture efficiency for a fixed cylinder was confronted to theoretical, experimental, and numerical data from prior studies.

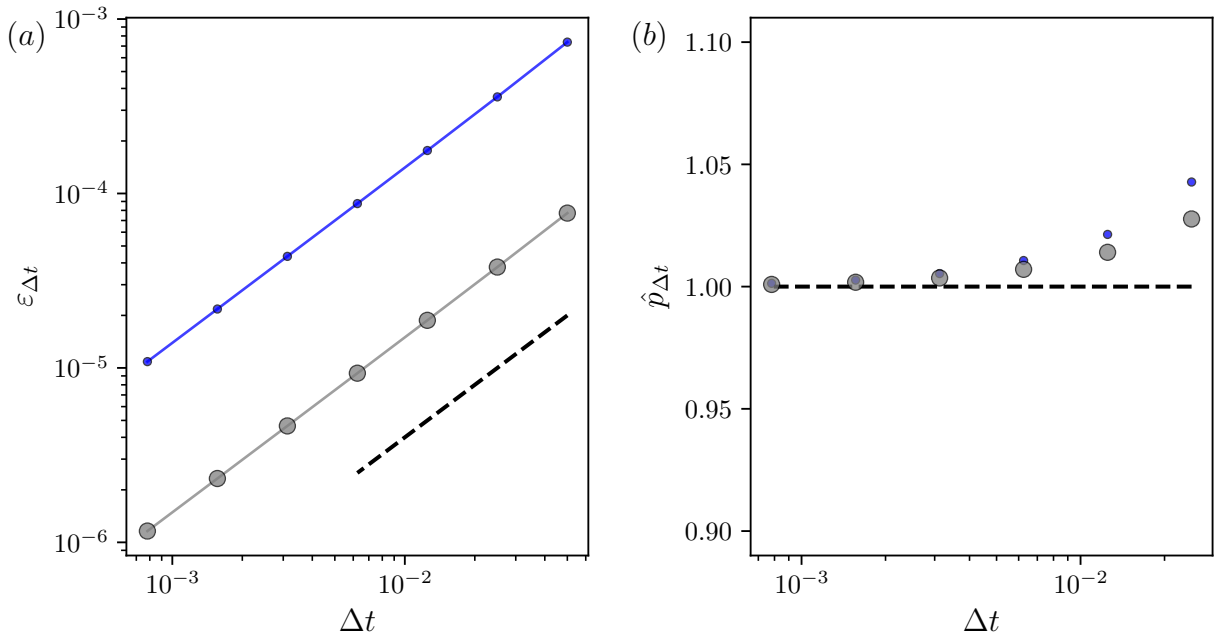

Figure 1: Verification of the code Paradvect for a small particle (·, $R = 0.01$) and a large particle (●, $R = 0.1$). In both cases, the flow is uniform and unidirectional, without obstacles, and the grid is the same. (a) Discretisation error using the norm L_2, defined in equation (1). (b) Observed order of accuracy using the Richardson extrapolation. The dashed lines refer to a linear variation.

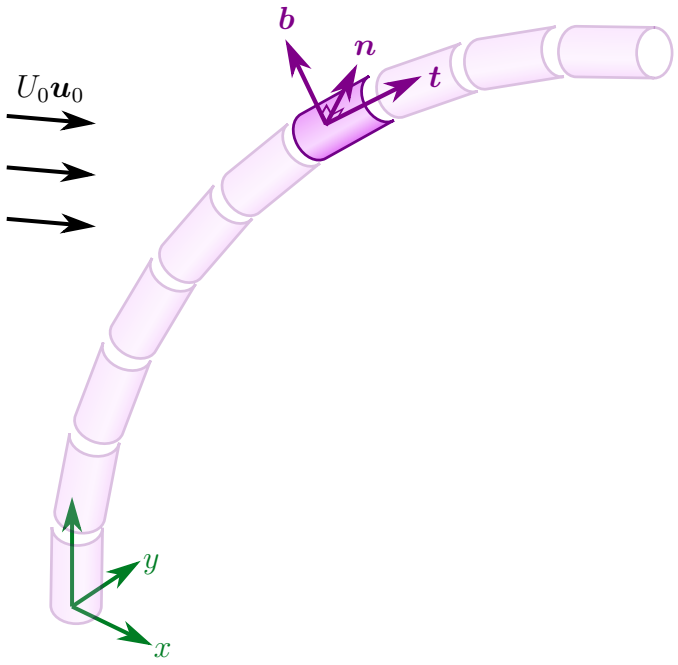

Figure 2: Illustration of a rod having a clamped end, within a fluid flow of upstream speed U_0 in the direction $\boldsymbol{u}_0$. The rod is meshed into elements of same length, each of them having a local material frame $(\boldsymbol{t}, \boldsymbol{n}, \boldsymbol{b})$.

2 Elastic rod dynamics

2.1 Kirchhoff equations

We consider an elastic, straight rod with a clamped end, of a mass per unit length m_l, length L, and circular cross-section of diameter D, as sketched in figure 2. This rod has a flexural rigidity EI and torsional rigidity $GJ = (2/3)EI$. We refer to a position in the rod by the arc length $s \in [0, L]$, and denote the position vector as $\boldsymbol{w}$.

We build the material frame, along the rod, from the tangential vector $\boldsymbol{t}$ defined as [Landau and Lifshitz, 1970]

$$\boldsymbol{t} = \frac{\partial \boldsymbol{w}}{\partial s}. \tag{3}$$

The rate of change of the tangential vector along the deformed profile of the rod is [Audoly and Pomeau, 2010]

$$\frac{\partial \boldsymbol{t}}{\partial s} = \boldsymbol{\Omega} \times \boldsymbol{t}. \tag{4}$$

The vector $\boldsymbol{\Omega}$ is called the Darboux vector, and quantifies the rate of rotation along the rod, or in other words, the curvature of the rod.

The second vector of the material frame is the normal vector, denoted $\boldsymbol{n}$, which also

varies as

$$\frac{\partial \boldsymbol{n}}{\partial s} = \boldsymbol{\Omega} \times \boldsymbol{n}. \tag{5}$$

The vector $\boldsymbol{t}$ is always orthogonal to $\boldsymbol{n}$ since

$$\frac{\partial(\boldsymbol{t} \cdot \boldsymbol{n})}{\partial s} = (\boldsymbol{\Omega} \times \boldsymbol{t}) \cdot \boldsymbol{t} + (\boldsymbol{\Omega} \times \boldsymbol{n}) \cdot \boldsymbol{n} = 0. \tag{6}$$

We complete the construction of the material frame with the binormal vector $\boldsymbol{b}$ defined as

$$\boldsymbol{b} = \boldsymbol{t} \times \boldsymbol{n}. \tag{7}$$

The constitutive equation we use is [Landau and Lifshitz, 1970, Audoly and Pomeau, 2010]

$$\begin{aligned} \boldsymbol{M} &= EI\boldsymbol{\Omega} + (GJ - EI)(\boldsymbol{\Omega} \cdot \boldsymbol{t})\boldsymbol{t} \\ &= EI\left[\boldsymbol{\Omega} - \frac{1}{3}(\boldsymbol{\Omega} \cdot \boldsymbol{t})\boldsymbol{t}\right], \end{aligned} \tag{8}$$

with $\boldsymbol{M}$ the internal moment. This is a general formulation that includes twist, as the product $\boldsymbol{\Omega} \cdot \boldsymbol{t}$ might be non-zero for a given load.

Finally, assuming that external moments are absent, the variation of the internal moment $\boldsymbol{M}$ and internal force $\boldsymbol{F}_{\text{int}}$ reads

$$\frac{\partial \boldsymbol{M}}{\partial s} = \boldsymbol{F}_{\text{int}} \times \boldsymbol{t} \tag{9}$$

$$\frac{\partial \boldsymbol{F}_{\text{int}}}{\partial s} = m_{\text{l}} \frac{\partial^2 \boldsymbol{w}}{\partial t^2} - \boldsymbol{f}_{\text{ext}}, \tag{10}$$

where $\boldsymbol{f}_{\text{ext}}$ is the total external force per unit length acting on the rod.

We non-dimensionalise the above equation via

$$\begin{gathered} \tilde{t} = \frac{t}{t_{\text{s}}}, \quad \tilde{s} = \frac{s}{L}, \quad \tilde{\boldsymbol{w}} = \frac{1}{L}\boldsymbol{w}, \quad \tilde{\boldsymbol{\Omega}} = L\boldsymbol{\Omega}, \\ \tilde{\boldsymbol{M}} = \frac{L}{EI}\boldsymbol{M}, \quad \tilde{\boldsymbol{F}}_{\text{int}} = \frac{L^2}{EI}\boldsymbol{F}_{\text{int}}, \quad \tilde{\boldsymbol{f}}_{\text{ext}} = \frac{L^3}{EI}\boldsymbol{f}_{\text{ext}}, \end{gathered} \tag{11}$$

with

$$t_{\text{s}} = L^2\sqrt{\frac{m_{\text{l}}}{EI}} \tag{12}$$

being a characteristic time for the structural deformation. The governing equations be-

come

$$\frac{\partial \tilde{\boldsymbol{w}}}{\partial \tilde{s}} = \boldsymbol{t}, \quad \frac{\partial \boldsymbol{t}}{\partial \tilde{s}} = \tilde{\boldsymbol{\Omega}} \times \boldsymbol{t}, \quad \frac{\partial \boldsymbol{n}}{\partial \tilde{s}} = \tilde{\boldsymbol{\Omega}} \times \boldsymbol{n},$$
$$\frac{\partial \tilde{\boldsymbol{M}}}{\partial \tilde{s}} = \tilde{\boldsymbol{F}}_{\text{int}} \times \boldsymbol{t}, \quad \frac{\partial \tilde{\boldsymbol{F}}_{\text{int}}}{\partial \tilde{s}} = \frac{\partial^2 \tilde{\boldsymbol{w}}}{\partial \tilde{t}^2} - \tilde{\boldsymbol{f}}_{\text{ext}}, \tag{13}$$

with

$$\tilde{\boldsymbol{M}} = \tilde{\boldsymbol{\Omega}} - \frac{1}{3}(\tilde{\boldsymbol{\Omega}} \cdot \boldsymbol{t})\boldsymbol{t}. \tag{14}$$

For a rod with a clamped end, the boundary conditions are

$$\boldsymbol{w}|_{s=0} = \boldsymbol{0}, \quad \boldsymbol{t}|_{s=0} = \left.\frac{\partial \boldsymbol{w}}{\partial s}\right|_{s=0} = \boldsymbol{t}_{\text{root}}, \quad \boldsymbol{n}|_{s=0} = (\boldsymbol{t}_{\text{root}} \times \boldsymbol{u}) / \left|\left|\boldsymbol{t}_{\text{root}} \times \boldsymbol{u}\right|\right|,$$
$$\boldsymbol{M}|_{s=L} = \boldsymbol{0}, \quad \boldsymbol{F}_{\text{int}}|_{s=L} = \boldsymbol{0}, \tag{15}$$

where $\boldsymbol{u}_0$ is the upstream flow direction. In dimensionless form, we get

$$\tilde{\boldsymbol{w}}|_{\tilde{s}=0} = \boldsymbol{0}, \quad \boldsymbol{t}|_{\tilde{s}=0} = \boldsymbol{t}_{\text{root}}, \quad \boldsymbol{n}|_{\tilde{s}=0} = (\boldsymbol{t}_{\text{root}} \times \boldsymbol{u}) / \left|\left|\boldsymbol{t}_{\text{root}} \times \boldsymbol{u}\right|\right|,$$
$$\tilde{\boldsymbol{\Omega}}|_{\tilde{s}=1} = \boldsymbol{0}, \quad \tilde{\boldsymbol{F}}_{\text{int}}|_{\tilde{s}=1} = \boldsymbol{0}. \tag{16}$$

2.2 External forces

2.3 Drag

Following the empirical work of Taylor [1952], the axial component of the drag is neglected, and only the components of the fluid velocity that are perpendicular to the rod generate load. The force that acts on an infinitesimal length $\mathrm{d}s$ expresses as

$$\mathrm{d}\boldsymbol{F}_{\text{D}} = \frac{1}{2} C_{\text{D}} D \rho_{\text{f}} \left(|\boldsymbol{U}_{\text{rel}} \cdot \boldsymbol{n}| \, (\boldsymbol{U}_{\text{rel}} \cdot \boldsymbol{n})\boldsymbol{n} + |\boldsymbol{U}_{\text{rel}} \cdot \boldsymbol{b}| \, (\boldsymbol{U}_{\text{rel}} \cdot \boldsymbol{b})\boldsymbol{b}\right) \mathrm{d}s \tag{17}$$

where C_{D} is the drag coefficient of the rod cross-section. The vector $\boldsymbol{U}_{\text{rel}}$ is the relative velocity of the flow relative to the rod

$$\boldsymbol{U}_{\text{rel}} = U_0 \boldsymbol{u}_0 - \frac{\partial \boldsymbol{w}}{\partial t}. \tag{18}$$

The dimensionless form of equation (18) is

$$\boldsymbol{u}_{\text{rel}} = \boldsymbol{u}_0 - \lambda \frac{\partial \tilde{\boldsymbol{w}}}{\partial \tilde{t}}. \tag{19}$$

The constant λ is

$$\lambda = \frac{L}{U_0 t_\mathrm{s}} = \frac{St\Gamma}{U_\mathrm{r}}, \tag{20}$$

with St the Strouhal number, $U_\mathrm{r} = StU_0 t_\mathrm{s}/D$ the reduced velocity, and $\Gamma = L/D$ the aspect ratio of the rod. Here λ gives an idea of the magnitude of the rod velocity with respect to the fluid speed: a small λ indicates a slow rod motion, whereas a large λ indicates a fast rod motion.

We deduce the drag per unit length

$$\boldsymbol{f}_\mathrm{D} = \frac{\partial \boldsymbol{F}_\mathrm{D}}{\partial s} = \frac{1}{2} C_\mathrm{D} D \rho_\mathrm{f} U_0^2 (|u_n|\, u_n \boldsymbol{n} + |u_b|\, u_b \boldsymbol{b}), \tag{21}$$

with

$$u_n = \boldsymbol{u}_\mathrm{rel} \cdot \boldsymbol{n} \quad \text{and} \quad u_b = \boldsymbol{u}_\mathrm{rel} \cdot \boldsymbol{b}. \tag{22}$$

Therefore, we obtain in dimensionless form

$$\tilde{\boldsymbol{f}}_\mathrm{D} = C_\mathrm{D} C_\mathrm{Y} (|u_n|\, u_n \boldsymbol{n} + |u_b|\, u_b \boldsymbol{b}). \tag{23}$$

The ratio

$$C_\mathrm{Y} = \frac{\rho_\mathrm{f} U_0^2 D L^3}{2EI} \tag{24}$$

is the Cauchy number, and compares the fluid-dynamic pressure to the elastic bending rigidity of the rod [de Langre, 2001].

2.4 Added mass

Regarding the added mass effect, we follow Leclercq and de Langre [2018] and Leclercq and de Langre [2018] and use the expression for slender structures proposed by Candelier et al. [2011] (notice the sign of the force and the relative velocity definition (18))

$$\boldsymbol{f}_\mathrm{A} = m_\mathrm{a} \left[U_0 \frac{\partial (u_n \boldsymbol{n} + u_b \boldsymbol{b})}{\partial t} + U_0^2 \frac{\partial u_t (u_n \boldsymbol{n} + u_b \boldsymbol{b})}{\partial s} - \frac{U_0^2}{2} \frac{\partial (u_n^2 + u_b^2) \boldsymbol{t}}{\partial s} \right], \tag{25}$$

with $m_\mathrm{a} = \pi \rho_\mathrm{f} D^2/4$ being the added mass per unit length. The dimensionless form of the added mass force is

$$\tilde{\boldsymbol{f}}_\mathrm{A} = \frac{\pi C_\mathrm{Y}}{2\Gamma} \left[\lambda \frac{\partial (u_n \boldsymbol{n} + u_b \boldsymbol{b})}{\partial \tilde{t}} + \frac{\partial u_t (u_n \boldsymbol{n} + u_b \boldsymbol{b})}{\partial \tilde{s}} - \frac{1}{2} \frac{\partial (u_n^2 + u_b^2) \boldsymbol{t}}{\partial \tilde{s}} \right]. \tag{26}$$

2.5 Vortex-induced lift

In the phenomenological wake-oscillator model of Facchinetti et al. [2004], the lift induced by vortices is perpendicular to the flow stream and initial rod axis. In our three-dimensional simulations, we fix the direction of the lift $\boldsymbol{u}_0^{\perp}$ as the normal to the plane defined by the flow and initial rod configuration

$$\boldsymbol{u}_0^{\perp} = (\boldsymbol{t}_{\text{root}} \times \boldsymbol{u}_0) / \left|| \boldsymbol{t}_{\text{root}} \times \boldsymbol{u}_0 \right|| . \tag{27}$$

The lift force can be expressed as

$$\boldsymbol{f}_{\text{VIV}} = \frac{1}{2} C_{\text{L}} D \rho_{\text{f}} U_0^2 u_b^2 \boldsymbol{u}_0^{\perp}, \tag{28}$$

where the time-fluctuating lift coefficient is defined as [Facchinetti et al., 2004]

$$C_{\text{L}} = \frac{C_{\text{L}}^0}{2} q. \tag{29}$$

The coefficient C_{L}^0 is the measured lift coefficient of a fixed cross-section during vortex shedding, and q is the fluctuating variable that verifies the van der Pol equation

$$\frac{\partial^2 q}{\partial t^2} + \varepsilon \left[\frac{2\pi St U_0 |u_b|}{D} \right] (q^2 - 1) \frac{\partial q}{\partial t} + \left[\frac{2\pi St U_0 |u_b|}{D} \right]^2 q = \frac{A}{D} \frac{\partial^2 \boldsymbol{w}}{\partial t^2} \cdot \boldsymbol{u}_0^{\perp}, \tag{30}$$

with $U_0 u_b$ being the binormal component of the upstream flow velocity, perpendicular to the rod. We take the same coupling constants $A = 12$ and $\varepsilon = 0.3$ as in Facchinetti et al. [2004], which give correct results even for slender flexible structures. Also, the fluid-dynamic coefficients in our simulations are equal to $C_{\text{D}} = 1.2$ and $C_{\text{L}}^0 = 0.3$, like in Facchinetti et al. [2004] and our DNS results with CADYF as well. Though, we take a smaller Strouhal number $St = 0.16$ because we compute flows of lower Reynolds numbers.

We non-dimensionalise the expression of the vortex-induced lift

$$\tilde{\boldsymbol{f}}_{\text{VIV}} = \frac{C_{\text{L}}^0 C_{\text{Y}}}{2} u_b^2 q \boldsymbol{u}_0^{\perp}, \tag{31}$$

and the van der Pol equation

$$\frac{\partial^2 q}{\partial \tilde{t}^2} + \varepsilon \omega_{\text{f}} |u_b| (q^2 - 1) \frac{\partial q}{\partial \tilde{t}} + \omega_{\text{f}}^2 u_b^2 q = \Gamma A \frac{\partial^2 \tilde{\boldsymbol{w}}}{\partial \tilde{t}^2} \cdot \boldsymbol{u}_0^{\perp}, \tag{32}$$

with

$$\omega_{\text{f}} = 2\pi St \frac{U_0 t_{\text{s}}}{D} = 2\pi U_{\text{r}}. \tag{33}$$

In the rest of this document we will drop the notation $\tilde{(.)}$ out of dimensionless quantities.

2.6 Solving method

We perform simulations using a backward Euler scheme. Initially, we assign the node positions of the mesh to the vector $\boldsymbol{w}|_{t=0,s} = \boldsymbol{w}_{\text{init}}(s)$. In FEniCS we extract directly the tangential vector of the initial configuration $\boldsymbol{t}_0$ of each element, then calculate the normal vector from

$$\boldsymbol{n}_{\text{init}} = (\boldsymbol{t}_{\text{init}} \times \boldsymbol{u}) / \left|\left|\boldsymbol{t}_{\text{init}} \times \boldsymbol{u}\right|\right|. \tag{34}$$

To calculate the initial value of the Darboux vector $\boldsymbol{\Omega}_{\text{init}}$ and internal stress $\boldsymbol{F}_{\text{int,init}}$, we cross-multiply the vector $\boldsymbol{t}_{\text{init}}$ with the equations (4), (5), and (9)

$$\boldsymbol{\Omega}_{\text{init}} = \boldsymbol{t}_{\text{init}} \times \frac{\partial \boldsymbol{t}_{\text{init}}}{\partial s} + (\boldsymbol{b}_{\text{init}} \cdot \frac{\partial \boldsymbol{n}_{\text{init}}}{\partial s})\boldsymbol{t}_{\text{init}}, \tag{35}$$

$$\boldsymbol{F}_{\text{int,init}} = \boldsymbol{t}_{\text{init}} \times \frac{\partial \boldsymbol{M}_{\text{init}}}{\partial s}. \tag{36}$$

The rod has zero initial velocity $\boldsymbol{v}_{\text{init}} = \boldsymbol{0}$, and subjected initially, at each node, to a random value of the lift fluctuation of order $q \sim 10^{-3}$.

We mesh the rod into uniform intervals. These are one-dimensional elements embedded in a three-dimensional space. We choose $\mathcal{P}_1$ Lagrange elements, and solve the nonlinear equations using the Newton method.

2.7 Verification

To verify the code, we consider the problem of a rod under a distributed load $\tilde{\boldsymbol{f}}_{\text{ext}} = \tilde{f}_0 \boldsymbol{u}_0$.

First we calculate the discretisation error ε_N between a fine grid with N elements and a coarse one with $N/2$ elements [Oberkampf and Roy, 2010]

$$\varepsilon_N = \left|\left|w_{0,N} - w_{0,N/2}\right|\right|_2 = \left[\frac{1}{N/2}\sum_{i=1}^{N/2} |w_{0,N}(s_i) - w_{0,N/2}(s_i)|^2\right]^{1/2}, \tag{37}$$

where the subscript $(.)_{.,N}$ refers to the solution under a mesh of N elements, and

$$w_0(s_i) = \boldsymbol{u}_0 \cdot \boldsymbol{w}|_{s_i}, \quad s_i = \frac{i}{N/2}. \tag{38}$$

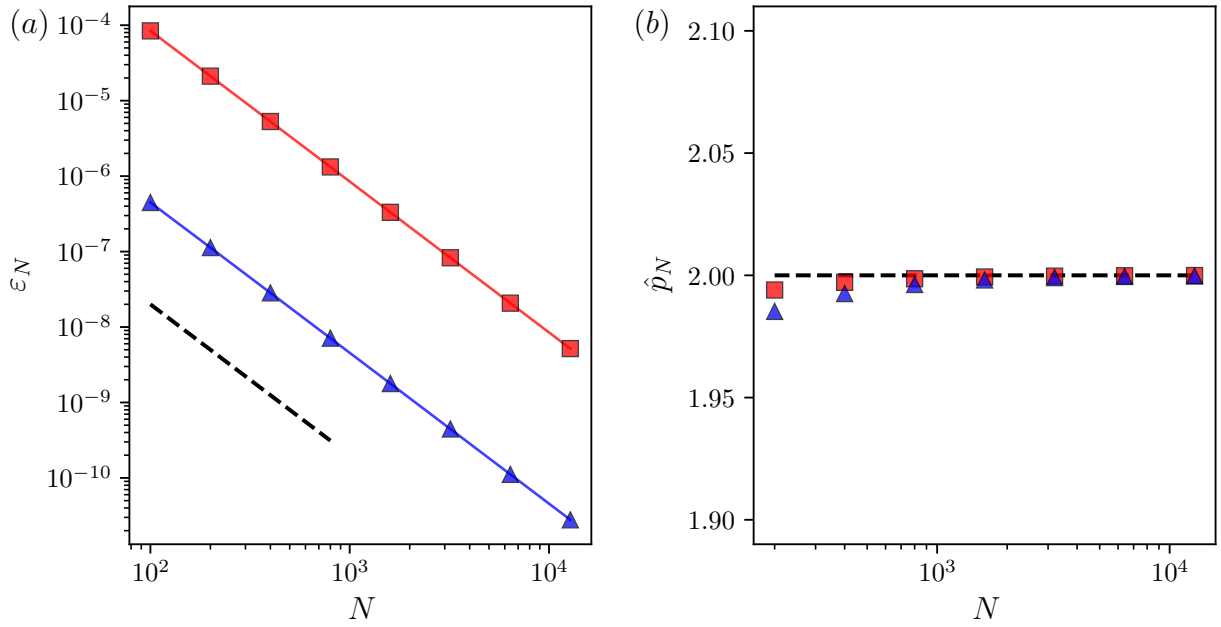

Figure 3: Code verification for the rod deflection under distributed load of small magnitude (▲, $\tilde{f}_0 = 0.1$) and a large magnitude (■, $\tilde{f}_0 = 10$). (a) Discretisation error using the norm L_2. (b) Observed order of accuracy using the Richardson extrapolation. The dashed lines refer to a quadratic variation.

We also calculate the observed order of accuracy $\hat{p}_N$ [Oberkampf and Roy, 2010]

$$\hat{p}_N = \frac{\log(\varepsilon_{N/2}/\varepsilon_N)}{\log(2)}. \tag{39}$$

The discretisation error is inversely proportional to the square of the element size, and the observed order of accuracy is close to 2, as expected from the use of Lagrange elements (see figure 3).

Now we fix the mesh ($N = 10$) and simulate the response of a rod under a distributed load between the instants $t_0 = 0$ and $t_\mathrm{f} = N_\mathrm{f}\Delta t$. We consider here the temporal discretisation error of the tip displacement

$$\varepsilon_{\Delta t} = ||w_{0,2\Delta t} - w_{0,\Delta t}||_2 = \left[2\Delta t \sum_{i=1}^{N_\mathrm{f}/2} |w^{\mathrm{tip}}_{0,2\Delta t}(t_k) - w^{\mathrm{tip}}_{0,\Delta t}(t_k)|^2\right]^{1/2}, \tag{40}$$

where the subscript $(.)_{.,\Delta t}$ refers to the solution with a time step equal to Δt, and

$$w^{\mathrm{tip}}_0(t_k) = \boldsymbol{u}_0 \cdot \boldsymbol{w}|_{t=t_k,s=1}, \quad t_k = k2\Delta t. \tag{41}$$

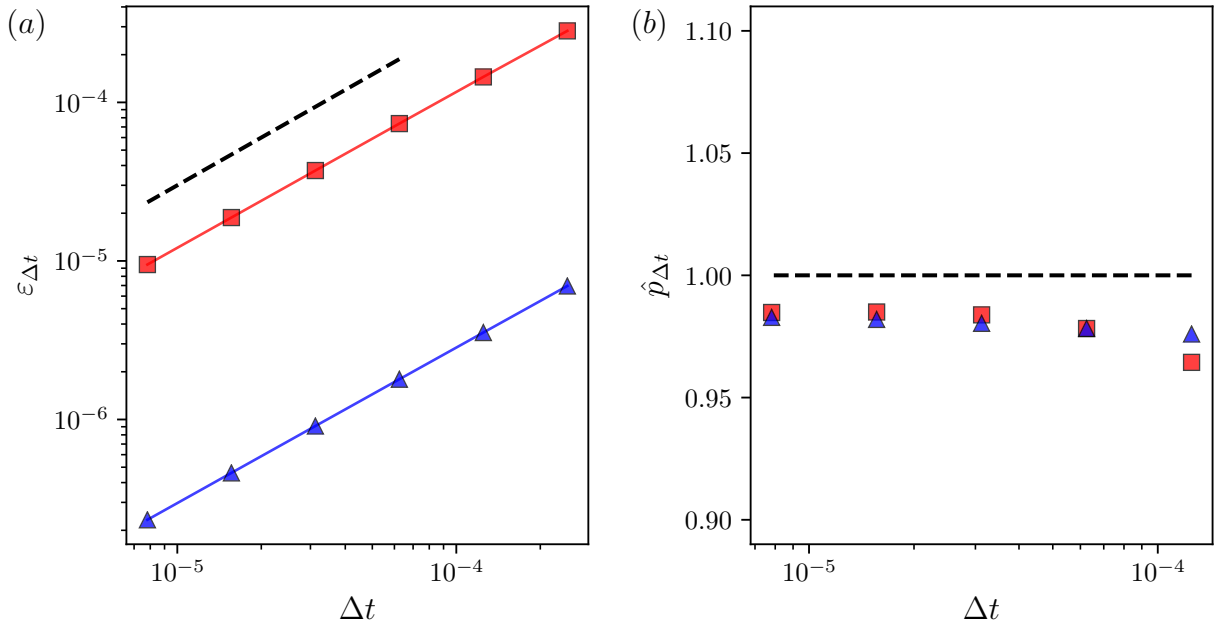

Figure 4: Code verification for the distributed load of small magnitude (▲, $\tilde{f}_0 = 0.1$) and a large magnitude (■, $\tilde{f}_0 = 10$). (a) Discretisation error using the norm L_2. (b) Observed order of accuracy using the Richardson extrapolation. The dashed lines refer to a linear variation.

Again, the observed order of accuracy $\hat{p}_{\Delta t}$ is given by

$$\hat{p}_{\Delta} = \frac{\log(\varepsilon_{\Delta}/\varepsilon_{2\Delta t})}{\log(2)}. \tag{42}$$

As seen in figure 4, the discretisation error varies linearly with the time step and the observed order of accuracy is close to 1, which is consistent with the use of a first order backward Euler scheme.

2.8 Validation

We simulate two benchmarks for the validation of static deformations. The first benchmark is the rod under a distributed load. For a range of loads $\tilde{f}_0 \boldsymbol{u}_0$, figure 5$(a)$ shows the numerical deflection of the rod at the tip

$$\delta_{\text{FEniCS}} = \boldsymbol{w}|_{s=1} \cdot \boldsymbol{u} \tag{43}$$

compared with the theoretical formula δ_{th} derived by Rohde [1952], which is based on series expansion. Taking the two leading terms in the approximation of δ_{th}, we found that the numerical results match well with the theoretical solution even for considerable

loads outside the linear regime $\delta \propto \tilde{f}_0$ ($|\delta_{\text{th}} - \delta_{\text{FEniCS}}| / \delta_{\text{th}} < 1.4\%$).

The second benchmark is a rod under drag. We evaluate the reconfiguration number, denoted $\mathcal{R}$, defined as the total drag F_{D} applied on the elastic rod scaled by the total drag on a rigid one

$$\mathcal{R} = F_{\text{D}} / \left(\frac{1}{2} \rho_{\text{f}} D L C_{\text{D}} U_0^2 \right). \tag{44}$$

In our code, we extract $\mathcal{R}$ as follows

$$\mathcal{R} = \int_0^1 \boldsymbol{u}_0 \cdot \boldsymbol{f}_{\text{D}} \mathrm{d}s / \left(\frac{1}{2} \rho_{\text{f}} D L C_{\text{D}} U_0^2 \right). \tag{45}$$

Gosselin et al. [2010] proposed a theoretical model, supported with experiments, that finds the reconfigured shape of a flexible thin, slender plate, and calculates the reconfiguration number for a wide range of Cauchy numbers. Since Kirchhoff equations govern both slender beams and rods, we compare our numerical results with the theoretical $\mathcal{R} - C_{\text{Y}}$ curve of Gosselin et al. [2010]. The comparison is shown in figure 5(b). Here again, our simulations lay well on the theoretical model ($|\mathcal{R}_{\text{th}} - \mathcal{R}_{\text{FEniCS}}| / \mathcal{R}_{\text{th}} < 3.1\%$).

2.9 Dynamic case

Leclercq and de Langre [2018] recorded the underwater motion of a thin plate fastened with an actuator that oscillates for different sets of pulsations Ω and displacements A. To transpose these experiments in our code, which fixes the clamped end, we make the rod sway back and forth by applying an oscillating flow

$$U(t) = U_0 \sin(\Omega t), \tag{46}$$

and choosing the corresponding velocity as

$$U_0 = \text{actuator displacement} \times \text{actuator pulsation} = A\Omega. \tag{47}$$

We consider low, moderate, and high pulsations $\omega = \Omega t_{\text{s}} = 0.38, 1.07, 2.01$, with three different actuator displacements $\alpha = A/L = 0.27, 0.46, 0.65$. We simulate the rod deformation over four periods and save the deformation profiles during the last period. We present experimental and numerical deformation profiles in figure 6. Results match well with the measurements of Leclercq and de Langre [2018], especially for low and moderate pulsations. The numerical deformation under high pulsation $\omega = 2.01$ is also comparable. There is a slight inclination in the cases $\alpha = 0.27$, which is absent from the measurements of Leclercq and de Langre [2018]. We presume it comes from experimental

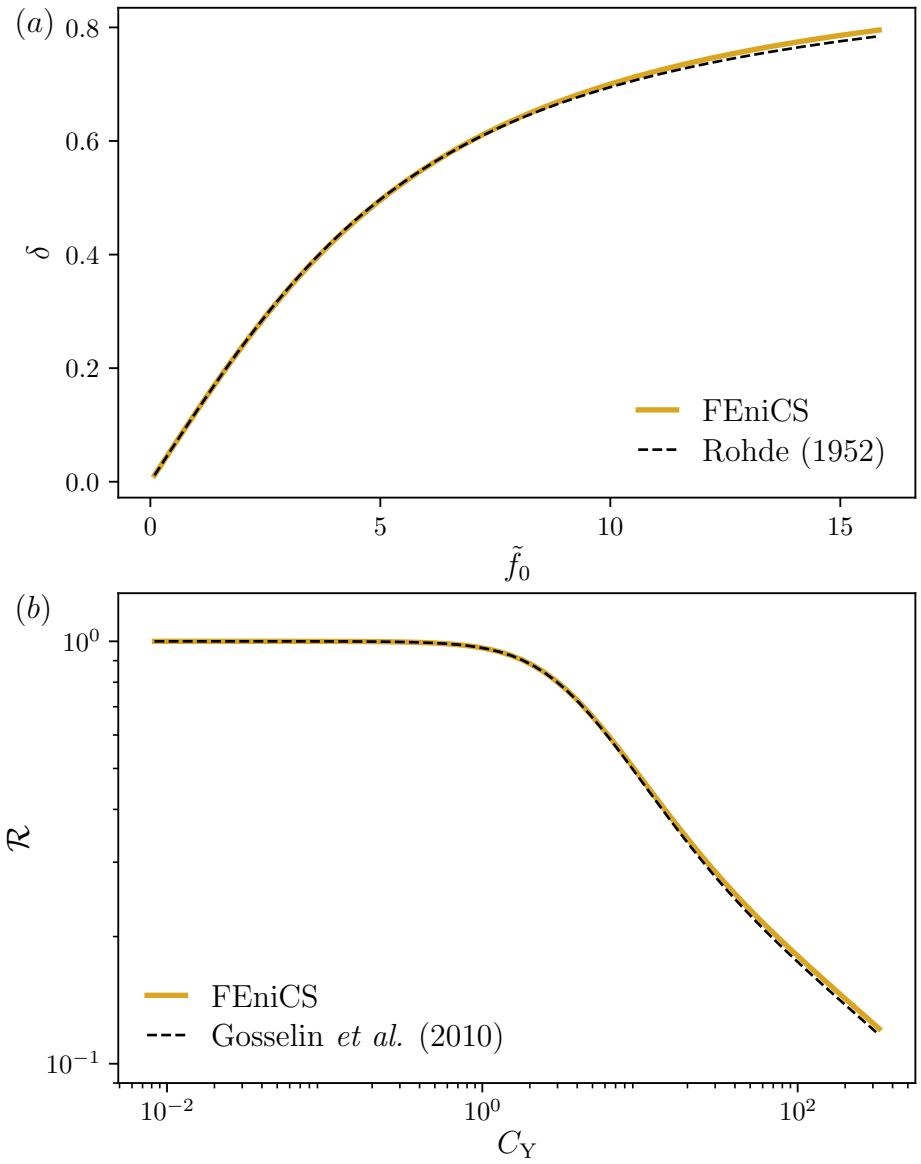

Figure 5: Comparison of the FEniCS solution with theoretical (a) maximum deflection of a rod under a distributed load and (b) reconfiguration number of a rod under drag.

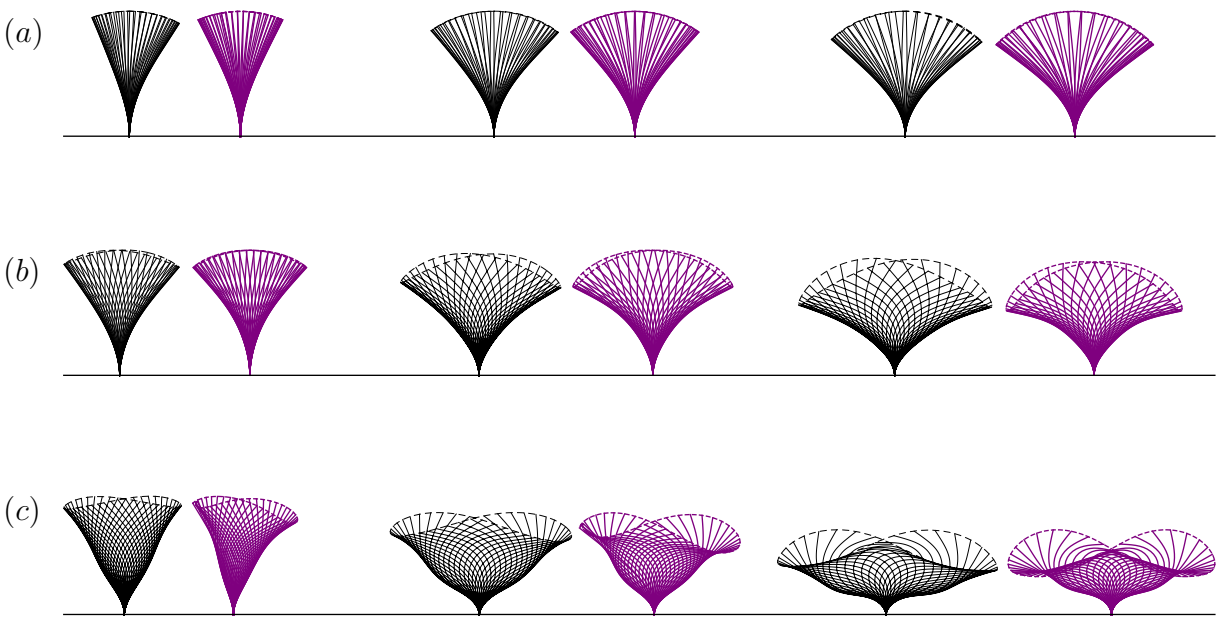

Figure 6: Deformation profiles of the plate experiments (black) of Leclercq and de Langre [2018] and rod simulations (purple) for the dimensionless flow pulsations $\omega = \Omega t_s$ equal to (a) 0.38, (b) 1.07, and (c) 2.01. In each case, the dimensionless actuator amplitude $\alpha = A/L$ goes from 0.27 (left), to 0.46 (middle), and 0.65 (right). The numerical equivalent case is a rod under an oscillating flow of upstream velocity in equation (46). The aspect ratio of the plate and rod is $\Gamma = 10$. The dashed lines represent the trajectory of the plate and rod tips.

features, due to important inertia effects that our model of hydrodynamic forces is unable to capture (non-symmetry is also present in experiments for the low pulsation and short displacement, and for high pulsation and moderate and high displacements, see top left, bottom centre, and bottom right in figure 6). This minor discrepancy, nevertheless, does not alter the overall comparison and the shapes remain fairly similar.

Table 1 summarises the values of the model parameters taken in the paper for rod simulations in section 2.

name	symbol	value
drag coefficient	C_{D}	1.2
lift coefficient (fixed cylinder)	C_{L}^0	0.3
Strouhal number	St	0.16
coupling parameters	(A, ε)	(12,0.3)
number of elements	N	30
time step	Δt	5×10^{-4}

Table 1: Values of the parameters used in the paper.

References

Paradvect. Paradvect (PARticle ADVECTion): a Python code to simulate the trajectory of particles advected by a fluid flow, June 2020. URL `https://zenodo.org/record/3981610`.

William L. Oberkampf and Christopher J. Roy. *Verification and Validation in Scientific Computing*. Cambridge University Press, October 2010. ISBN 978-1-139-49176-1.

Mouad Boudina, Frédérick P. Gosselin, and Stéphane Étienne. Direct interception or inertial impaction? A theoretical derivation of the efficiency power law for a simple and practical definition of capture modes. *Physics of Fluids*, 32(12):123603, December 2020. ISSN 1070-6631. doi: 10.1063/5.0030891.

L. D. Landau and E. M. Lifshitz. *Theory of Elasticity*. Pergamon Press, January 1970. ISBN 978-0-7506-2633-0.

Basile Audoly and Yves Pomeau. *Elasticity and Geometry: From hair curls to the nonlinear response of shells*. Oxford University Press, Oxford ; New York, August 2010. ISBN 978-0-19-850625-6.

Geoffrey Ingram Taylor. Analysis of the swimming of long and narrow animals. *Proceedings of the Royal Society of London. Series A. Mathematical and Physical Sciences*, 214(1117):158–183, August 1952. doi: 10.1098/rspa.1952.0159. URL `https://royalsocietypublishing.org/doi/abs/10.1098/rspa.1952.0159`. Publisher: Royal Society.

Emmanuel de Langre. *Fluides et solides*. Editions Ecole Polytechnique, 2001. ISBN 978-2-7302-0833-8.

Tristan Leclercq and Emmanuel de Langre. Reconfiguration of elastic blades in oscillatory flow. *Journal of Fluid Mechanics*, 838:606–630, March 2018. ISSN 0022-1120, 1469-7645. doi: 10.1017/jfm.2017.910. URL `https://doi.org/10.1017/jfm.2017.910`.

Tristan Leclercq and Emmanuel de Langre. Vortex-induced vibrations of cylinders bent by the flow. *Journal of Fluids and Structures*, 80:77–93, July 2018. ISSN 0889-9746. doi: 10.1016/j.jfluidstructs.2018.03.008. URL `http://www.sciencedirect.com/science/article/pii/S0889974617307764`.

Fabien Candelier, Frederic Boyer, and Alban Leroyer. Three-dimensional extension of Lighthill's large-amplitude elongated-body theory of fish locomotion. *Journal of Fluid Mechanics*, 674:196–226, May 2011. ISSN 1469-7645, 0022-1120. doi:

10.1017/S002211201000649X. URL https://doi.org/10.1017/S002211201000649X. Publisher: Cambridge University Press.

M. L. Facchinetti, E. de Langre, and F. Biolley. Coupling of structure and wake oscillators in vortex-induced vibrations. *Journal of Fluids and Structures*, 19(2):123–140, February 2004. ISSN 0889-9746. doi: 10.1016/j.jfluidstructs.2003.12.004. URL http://www.sciencedirect.com/science/article/pii/S0889974603001853.

F. Rohde. Large deflections of a cantilever beam with uniformly distributed load. *Quarterly of Applied Mathematics*, 11(3):337–338, 1952.

Frédérick Gosselin, Emmanuel de Langre, and Bruno A. Machado-Almeida. Drag reduction of flexible plates by reconfiguration. *Journal of Fluid Mechanics*, 650:319, May 2010. ISSN 0022-1120, 1469-7645. doi: 10.1017/S0022112009993673. URL http://www.journals.cambridge.org/abstract_S0022112009993673.